

## Learning from data: A post classification method for annual land cover analysis in urban areas



Shishi Liu<sup>a</sup>, Hang Su<sup>a</sup>, Guofeng Cao<sup>b,c</sup>, Shanqin Wang<sup>a</sup>, Qingfeng Guan<sup>d,e,\*</sup>

<sup>a</sup> School of Resources and Environment, Huazhong Agricultural University, Wuhan, Hubei 430070, China

<sup>b</sup> Department of Geosciences, Texas Tech University, Lubbock, TX 79409, United States

<sup>c</sup> Center for Geospatial Technology, Texas Tech University, Lubbock, TX 79409, United States

<sup>d</sup> School of Geography and Information Engineering, China University of Geosciences (Wuhan), Wuhan, Hubei 430074, China

<sup>e</sup> National Engineering Research Center of GIS, China University of Geosciences (Wuhan), Wuhan, Hubei 430074, China

### ARTICLE INFO

#### Keywords:

Annual land cover change detection

Spatio-temporal land cover filter

Urban area

### ABSTRACT

Annual analyses of land cover dynamics in urban areas provide a thorough understanding of the urbanization effects on environment and valuable information for the improvement of urban growth modeling. However, most current studies focus on major land cover changes, such as urbanization and vegetation loss. The most feasible way to evaluate the complex interactions among different land cover types is the post-classification change detection, but the temporal inconsistency in the time series of land cover maps impedes the high-frequency and long-term analyses. This study proposed a spatio-temporal land cover filter (STLCF) to remove the illogical land cover change events in the time series of land cover maps, and analyzed the annual land cover dynamics in urban areas. The knowledge of illogical land cover change events was ‘learned’ from the land cover maps through the spatio-temporal transition probability matrix, instead of experts’ knowledge. The illogical change was modified with the land cover of the maximum probability calculated from the naïve Bayesian equation. The STLCF was tested in Wuhan, a typical densely urbanized Chinese city. The annual land cover maps from 2000 to 2013 were derived from multi-date Landsat images using the Decision Tree (DT) classifier. Results showed that the STLCF improved the mean overall accuracy of annual change detection by about 6%. Additionally, the amount of land cover trajectories with unrealistically frequent changes was significantly decreased. During the study period, 7.86% of the pixels experienced one land cover change, and about 0.57% of the pixels experienced land cover changes more than once. The annual analyses demonstrated the non-linear increasing trend in urbanization as well as the corresponding trend in vegetation loss in the study area. We also found the conversion from built-up areas to vegetation near rivers and lakes and in the reserves and rural areas, mainly caused by the restoration of built-up areas to the park or green belt/wedges along rivers and new roads in the metropolitan areas, and to the cropland and woods in the rural areas. Results of this study showed the importance of the spatio-temporal consistency check with knowledge derived from land cover maps of the study area, which facilitates the annual analyses of major and subtle land cover dynamics in urban areas.

### 1. Introduction

Accurate land cover maps in urban areas are important inputs of urban growth models (Guan et al., 2016; Dong et al., 2018) and hydrology models (Zomlot et al., 2017). They are also vital for monitoring, understanding, and predicting the effects of urbanization on public health (Gong et al., 2012), urban climate (Georgescu et al., 2014), and carbon sequestration (Churkina, 2008).

In the last three decades, important progress has been made in accurately mapping urban areas with remote sensing methods (Woodcock

and Ozdogan, 2012; Schneider et al., 2010; Liu et al., 2018). Studying urban systems requires land cover maps that are both sufficiently dense and extensive in time to adequately capture dynamics of a complex system. Attempts have been made to map urban areas annually during a long period (e.g. over a decade), especially with the free release of the Landsat Archive in 2008. Seto and Fragkias (2005) quantified the annual rate of land cover change for four cities in southern China, using ten classified Landsat Thematic Mapper images acquired from 1988 to 1999. Sexton et al. (2013) mapped the annual continuous fields of impervious surface cover in the Washington, D.C.-Baltimore

\* Corresponding author at: School of Geography and Information Engineering, China University of Geosciences (Wuhan), Wuhan, Hubei 430074, China.  
E-mail address: [guanqf@cug.edu.cn](mailto:guanqf@cug.edu.cn) (Q. Guan).

megalopolis from 1984 to 2010 using time series of Landsat images. Li et al. (2015) mapped the annual urban dynamics of Beijing from 1984 to 2013 using Landsat images. He et al. (2017) produced the annual land use and land cover maps of China from 1982 to 2013 using the Normalized Difference Vegetation Index (NDVI) data of the Advanced Very High Resolution Radiometer (AVHRR) Global Inventory Modelling and Mapping Studies (GIMMS). The long-term and high-frequency characterization of urban areas provides high-order complexities of land cover dynamics.

Annual analyses of land cover dynamics in urban areas help address some fundamental questions of where, when, how long, and how much urban land change has occurred, which will facilitate the improvement in urban land use and land cover change models and provide a thorough understanding of the urbanization effects on environment (Guan et al., 2016). Unlike the natural vegetated area where vegetation loss and gain can be detected using the break points of vegetation index (e.g. NDVI) trajectory (Jamali et al., 2015), land cover changes in urban areas are more complicated, with inter-class conversions among multiple land cover types. Because of the complexities, the limited current studies of annual urban dynamics mainly focus on major land cover changes. Chai and Li (2018) proposed a method of extracting urban expansion using annual Landsat time series data. The method included the one-class (urban) classification and the subsequent spatio-temporal refinement. Results showed the improvement in the classification accuracy through the proposed method, and emphasized the importance of the spatial-temporal consistency check for annual urban land cover maps. Li et al. (2018) developed a temporal approach to detect the turning years of the start and end of change from vegetation, water, and bare land to urban, using the time series of Landsat data from 1985 to 2015. The approach achieved reliable change detection results, but it was more preferred in the small- and medium-size cities with gradual changes, because it cannot detect multi-phases changes that are commonly occurred in the developing countries.

The post-classification change detection method is the most feasible way to annually analyze the complex inter-class conversions in urban areas. However, the temporal inconsistency issue in the multi-date land cover maps, resulted from mis-registration and mis-classification, impedes the applications of the from-to post classification method. The temporal inconsistency issue can be solved either by using a spatio-temporal Markovian classifier to produce temporal-consistent land cover maps in the first place or applying a temporal filter to modifying the unrealistic land cover transitions on the existing land cover maps. The spatio-temporal Markovian method couples the existing classifier (e.g. support vector machine classifier, SVM) with the Markov Random Field (MRF) model to map land cover types using both spectral information and spatio-temporal contextual information (Liu and Cai, 2012; Cai et al., 2014; Wehmann and Liu, 2015; Wang et al., 2015). Studies have shown that the spatio-temporal Markovian method can improve the overall classification accuracy and temporal consistency. In this method, the exclusion of the illogical land cover changes was based on expert knowledge (Liu and Cai, 2012). The method needs complicated parameterizations. The overall accuracy and the temporal consistency of the multi-temporal land cover maps largely depend on the parameterizations of the spatio-temporal Markovian model (Wehmann and Liu, 2015).

The temporal filter method uses a moving time window to examine the temporal sequence of land cover types of each pixel. Generally, the temporal filter detects the unrealistic land cover transitions either based on a look-up table from the expert knowledge (Clark et al., 2010; He et al., 2017; Chai and Li, 2018) or based on the calculated probability (Sexton et al., 2013; Li et al., 2015). For the temporal filter using a look-up table, the detected unrealistic land cover types are simply replaced with the land cover type of the previous year (Clark et al., 2010; He et al., 2017). Processing is more complicated for the temporal filter method based on probability. Sexton et al. (2013) developed a temporal filter that recalculated each class's probability as the maximum of its

probability at the current year versus the square-root of the joint probability in the year before and after, and the pixel was assigned with the label of the class with the maximum probability. The method was effective for temporal consistency check, but it did not take into account the spatial context. Li et al. (2015) proposed an iterative temporal filtering method to remove the illogical conversion from urban to non-urban in the land cover trajectory, using the temporal consistency probability. Overall, the temporal filter method is simple to implement and effective to remove a few cases of unrealistic land cover transitions. However, removing the illogical land cover conversions based on the expert knowledge may miss the important but subtle land cover changes in the urban areas. For example, most studies assume that the built-up areas are irreversible, but in a lot of cities the built-up areas can be converted to vegetated areas either due to restoration or urban shrinkage (Derkzen et al., 2017). The illogical land cover conversion should be better defined from the land cover maps of the study area, which reflect the land cover change process shaped by local policies and environment.

The objectives of this research are (1) to develop a spatio-temporal land cover filter (STLCF) to remove the illogical land cover change events, in which the knowledge of illogical change events is ‘learned’ from the land cover maps of the study area, instead of experts’ knowledge; and (2) to analyze the annual dynamics of land cover changes in the urban area.

## 2. Methods

### 2.1. Study area

This study was conducted in Wuhan ( $113^{\circ}41'E \sim 115^{\circ}05'E$ ,  $29^{\circ}50'N \sim 31^{\circ}22'N$ ), the capital of Hubei Province, China, because it is a typical densely urbanized Chinese city. Wuhan is located in central China and covers an area of  $8494.41\text{ km}^2$ . It lies at the intersection of Yangtze and Han rivers, and contains over 150 lakes and 70 parks. Natural vegetation is composed primarily of broadleaf trees.

Wuhan is among the fastest growing cities in China, and has been experiencing rapid urban expansions in the recent decade. The urban area in Wuhan increased from  $4.19 * 10^4\text{ ha}$  in 1988 to  $49.39 * 10^4\text{ ha}$  in 2011 (Tan et al., 2014). Wuhan comprises 13 districts with the total population approaching 10.4 million. The study area includes 11 districts of Wuhan, covering the whole metropolitan area and within one tile of Landsat images (Fig. 1).

### 2.2. Landsat images

The annual land cover maps of the study area were generated from Landsat surface reflectance image (path 123 row 039) from 2000 to 2013 (obtained from the US Geological Survey (USGS) Earth Resources Observation Systems (EROS) data center (<https://earthexplorer.usgs.gov>)). 100 Landsat images with cloud cover of less than 20% were used in this study. Since the study considered land cover types within both spatial and temporal neighborhood, to simplify the spatio-temporal transition probability matrix used in this study, we only classified the study area into built-up areas, bare land, vegetation, and water bodies.

The summer scene can maximize the spectral differences among these land cover types (Li et al., 2015). One clear Landsat image (cloud cover of less than 10%) acquired between April and September was selected as the base scene for each year to create the land cover map. To facilitate the differentiation of land cover types, particularly considering the crop rotation in the study area, NDVI calculated from multi-date clear Landsat images (cloud cover of less than 20%) within a year were also used for classification (Fig. 2). The Scan Line Corrector (SLC)-off effect (which results in missing data lines in the image) was evident within some of the ETM + scenes. 37 ETM + scenes went through the gap-filling using the method developed by Scaramuzza et al. (2004).

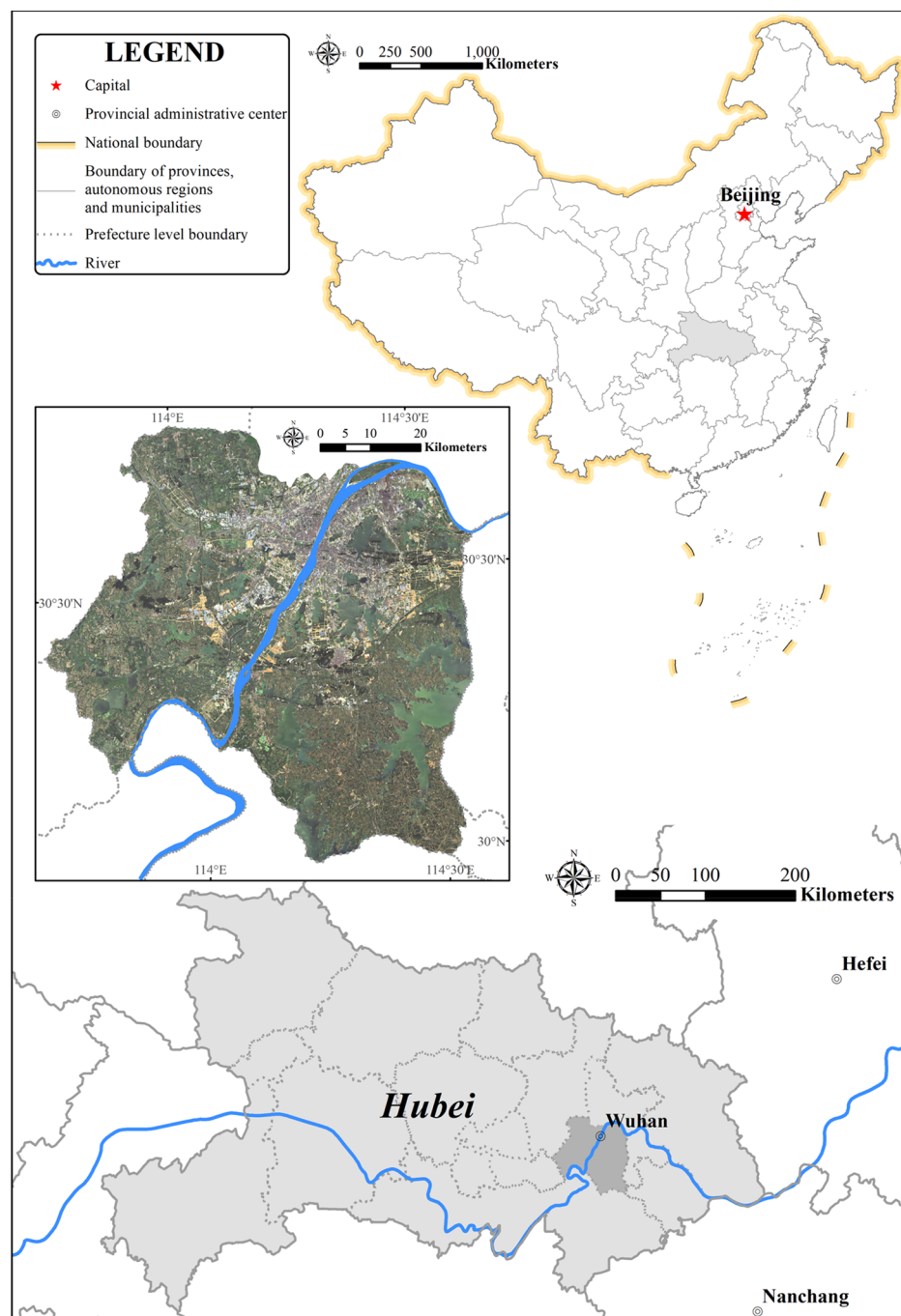


Fig. 1. Location of the study area.

### 2.3. Initial classification

Decision tree (DT) was employed to classify the study area into built-up areas, vegetation, water bodies, and bare land. In this study, built-up areas were defined as sites which are occupied by a particular non-vegetative, human-constructed physical structure, including buildings, streets, and impervious surfaces (Schneider, 2012; Chai and Li, 2018). Areas covered by vegetation or water, for example, a park or greenbelt, were not considered as urban land, even if they may be a part of urban space.

DT classification algorithm is a non-parametric supervised learning method, and has been shown to be superior to traditional Bayesian methods for discriminating complex hierarchical patterns in satellite data (Friedl et al., 2010; Schneider, 2012). In this study, the land cover

map of each year was created by the DT algorithm C4.5 (Friedl et al., 2010; Schneider, 2012), using the spectra of the base image and the NDVI derived from multi-date images within a year as inputs. The incorporation of multi-date NDVI can improve the differentiation between vegetation and the other land cover types, because NDVI values of built-up areas, bare land, and water were low in the year round whereas NDVI values reached the maximum at some point in the year for vegetation.

To train the DT classifier and validate classification results, approximately 2000 pixels were randomly collected as samples for each image through the visual interpretation of Landsat images, with the help of a 2013 summer image of WorldView-2, high-resolution images in Google Earth, and field observations. Samples were then randomly divided into two sub-samples for model training (70% of samples) and

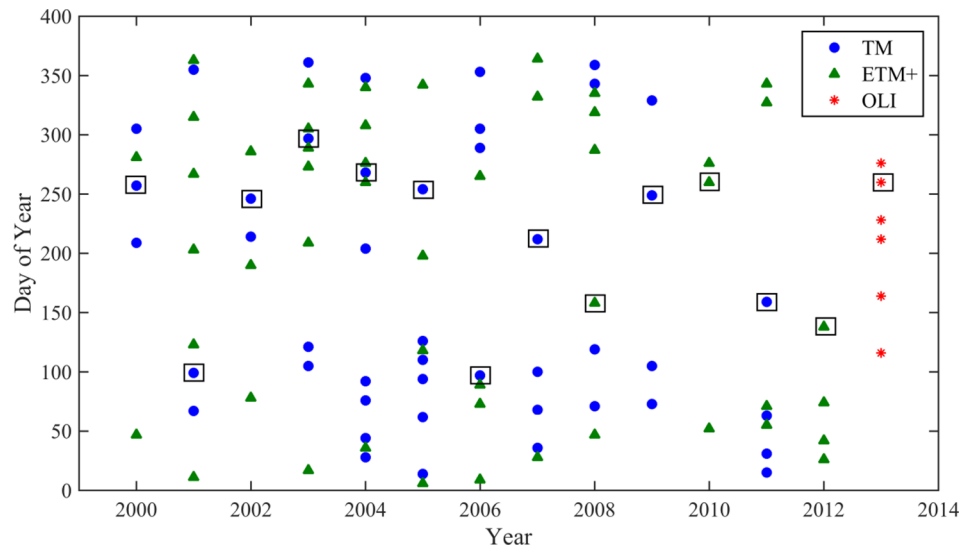


**Fig. 2.** The distribution of Landsat TM, ETM+, and OLI images used in the classification. The base images are marked with rectangles.

validation of classification accuracy (30% of samples). The overall accuracy of classification was calculated for each year to evaluate accuracy on the thematic dimension.

#### 2.4. Development of the STLCF

To implement the STLCF, a spatio-temporal transition probability matrix needs to be derived from the initial classifications. This spatio-temporal transition probability matrix provides the transition probability between land cover types in the given spatio-temporal context, and is served as a look-up table to identify and modify the unrealistic land cover transitions. The algorithm then iteratively scans the land cover sequence of each pixel and modifies the unrealistic transitions. In each iteration, if the land cover transition probability from year  $t - 1$  to year  $t$  was smaller than the predefined threshold, the land cover type at year  $t$  is modified to the land cover type with the maximum joint transition probability. At the end of each iteration, the land cover trajectories are summarized. The iterative modification ends till the cumulative percentage of the top 20 land cover trajectories reaching

complexity. Given a pixel and the associated pre-defined spatial moving neighborhood, we use the dominant land cover type, the type shared by the maximum number of pixels in the neighborhood, to build the temporal transition matrix under the context of the dominant type. Specifically, considering two land cover maps acquired at year  $t - 1$  and  $t$ ,  $C(t - 1)$  and  $C(t)$  denote the land cover types of a pixel  $u$  at  $t - 1$  and  $t$  respectively;  $N_{t-1}(u)$  denotes the spatial neighborhood of pixel  $u$  at  $t - 1$ . If more than one class had the same maximum number of pixels in the neighborhood, we randomly selected one of them as the dominant land cover type. In this study the spatial neighborhood  $N_{t-1}(u)$  was defined by  $3 \times 3$  pixels (refer to Section 4.2 for the discussion about the different spatial window sizes). The transition probability for pixel  $u$  from  $t - 1$  to  $t$  was calculated, given the dominant land cover type within the spatial neighborhood  $N_{t-1}(u)$  (Fig. 4). Therefore, for a land cover map with four types  $\{\omega_1, \omega_2, \omega_3, \omega_4\}$ , the spatio-temporal transition probability matrix includes four sub-matrices, specifying the transition probabilities from  $t - 1$  to  $t$  when the dominant land cover type within the spatial neighborhood  $N_{t-1}(u)$  is  $\omega_1, \omega_2, \omega_3$ , and  $\omega_4$  respectively:

$$M_{\omega_k} = \begin{pmatrix} P(C(t) = \omega_1 | C(t-1) = \omega_1) & P(C(t) = \omega_2 | C(t-1) = \omega_1) & P(C(t) = \omega_3 | C(t-1) = \omega_1) & P(C(t) = \omega_4 | C(t-1) = \omega_1) \\ P(C(t) = \omega_1 | C(t-1) = \omega_2) & P(C(t) = \omega_2 | C(t-1) = \omega_2) & P(C(t) = \omega_3 | C(t-1) = \omega_2) & P(C(t) = \omega_4 | C(t-1) = \omega_2) \\ P(C(t) = \omega_1 | C(t-1) = \omega_3) & P(C(t) = \omega_2 | C(t-1) = \omega_3) & P(C(t) = \omega_3 | C(t-1) = \omega_3) & P(C(t) = \omega_4 | C(t-1) = \omega_3) \\ P(C(t) = \omega_1 | C(t-1) = \omega_4) & P(C(t) = \omega_2 | C(t-1) = \omega_4) & P(C(t) = \omega_3 | C(t-1) = \omega_4) & P(C(t) = \omega_4 | C(t-1) = \omega_4) \end{pmatrix} \quad (1)$$

99.90%. The flowchart of the spatio-temporal land cover filtering is illustrated in Fig. 3.

##### 2.4.1. Spatio-temporal transition probability matrix

The STLCF identifies and modifies the unrealistic land cover transitions in a spatial and temporal context. The concept of spatial transition probability or transiogram (Li, 2006), an extension of the traditional probability in a spatial setting, has been used for modeling the complex geospatial patterns of categorical data (Li, 2007; Cao et al., 2011). Similarly, the spatial transition probability can be further extended into a spatio-temporal setting to characterize the land cover change trajectory. This spatio-temporal extension, however, will dramatically increase the computational complexity and render it computationally unsuitable for large remote sensing imagery analysis.

In this study, we use a practically efficient approach to model land use transitions while adequately taking into account the spatial and temporal contexts and at the same time mitigating the computation

where  $k = 1, 2, 3, 4$  and  $\omega_k$  denotes the dominant land cover type within the neighborhood,  $C(t - 1)$  and  $C(t)$  are the land cover types of the pixel  $u$  at year  $t - 1$  and  $t$  respectively, and  $P(\cdot|\cdot)$  is the transition probability. For example, given the dominant land cover type within the neighborhood of pixel  $u$  at year  $t - 1$  is  $\omega_k$ ,  $P(C(t) = \omega_j | C(t-1) = \omega_i)$  is the transition probability of pixel  $u$  from type  $\omega_1$  at year  $t - 1$  to type  $\omega_2$  at year  $t$ . The transition probability of the sub-matrix  $M_{\omega_k}$  is calculated based on the annual land cover maps of the study period:

$$P(C(t) = \omega_j | C(t-1) = \omega_i) = \frac{\sum (C(t-1) = \omega_i \text{ AND } C(t) = \omega_j)}{\sum C(t-1) = \omega_i} \quad (2)$$

where  $\sum (C(t-1) = \omega_i \text{ AND } C(t) = \omega_j)$  is the total number of pixels with the land cover type  $\omega_i$  ( $i = 1, 2, 3, 4$ ) at year  $t - 1$  converting to  $\omega_j$  ( $j = 1, 2, 3, 4$ ) at year  $t$  when the dominant land cover type within the neighborhood  $N_{t-1}(u)$  is  $\omega_k$  ( $k = 1, 2, 3, 4$ );  $\sum C(t-1) = \omega_i$  is the total number of pixels that are classified as land cover type  $\omega_i$  at year  $t - 1$ .

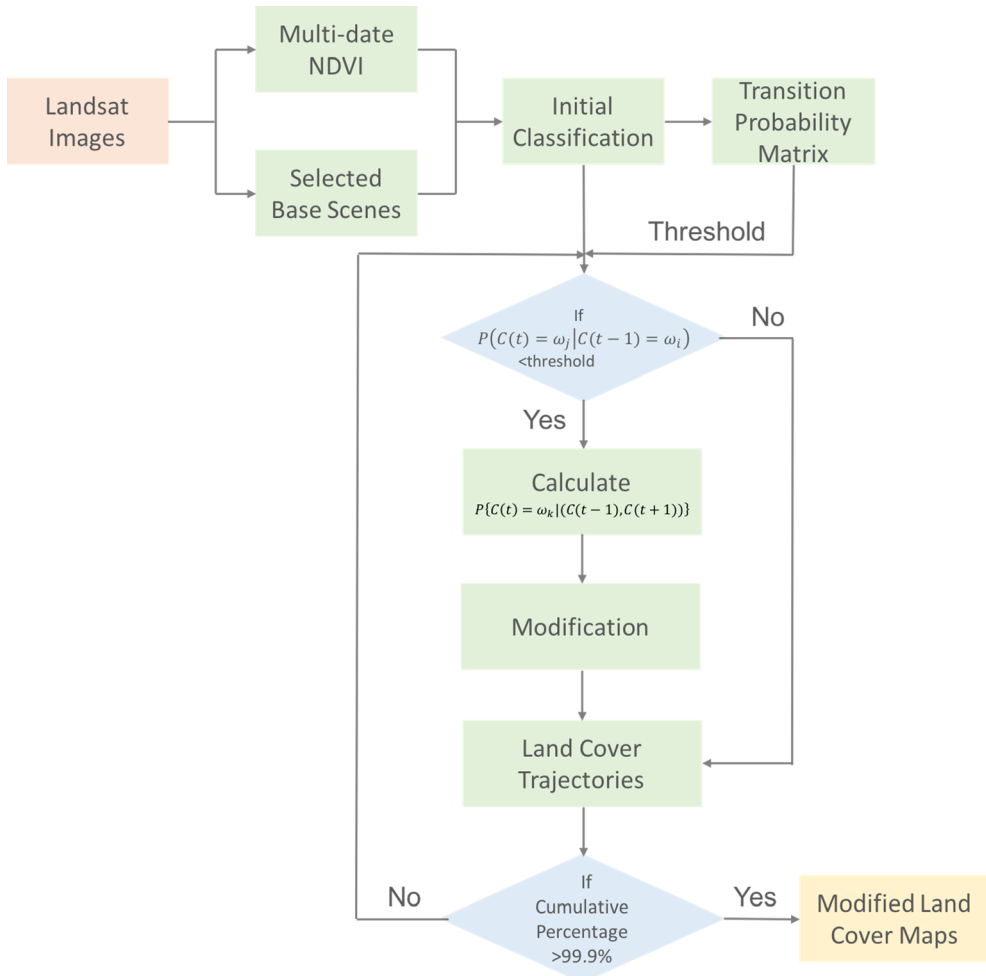


**Fig. 3.** The flowchart of the STLCF.  $P(C(t) = \omega_j | C(t-1) = \omega_i)$  is the land cover transition probability from land cover type  $\omega_i$  at year  $t-1$  to type  $\omega_j$  at year  $t$  (refer to Eq. (2) for details).  $P\{C(t) = \omega_k | (C(t-1), C(t+1))\}$  is the joint transition probability at year  $t$  given the land cover type at year  $t-1$  ( $C(t-1)$ ) and the land cover type at year  $t + 1$  ( $C(t+1)$ ) (refer to Eq. (3) for details).

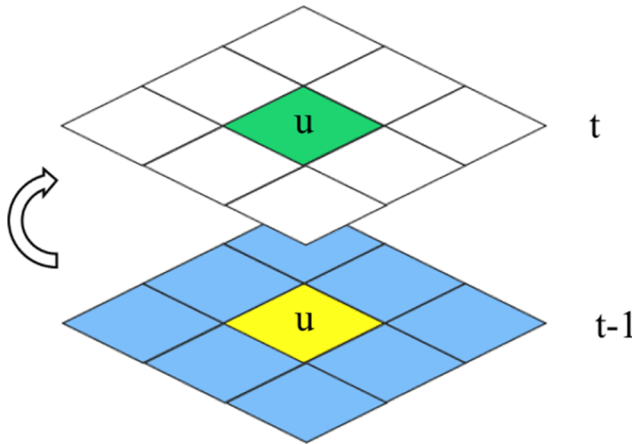


**Fig. 4.** The spatio-temporal neighborhood of a given pixel ( $u$ ). The  $3 \times 3$  spatial neighborhood of pixel  $u$  (including pixel  $u$ ) is in blue. Pixel  $u$  of the previous year ( $t-1$ ) is in yellow, and pixel  $u$  of the current year ( $t$ ) is in green. (For interpretation of the references to colour in this figure legend, the reader is referred to the web version of this article.)

#### 2.4.2. Iterative modification

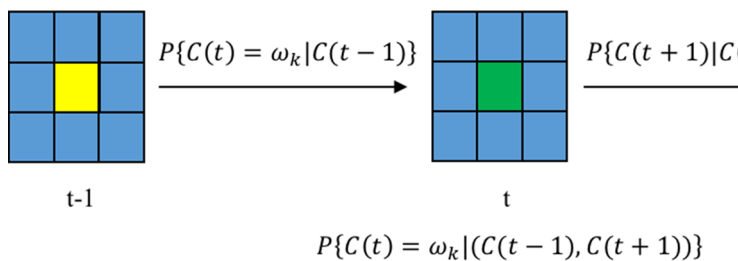
The algorithm then iteratively scans the land cover sequence of each pixel and modifies the unrealistic transitions. In each iteration, the land cover transitions with small probabilities are identified as the

unrealistic land cover transitions that need to be corrected in the following steps. As land cover change in time is a relatively rare phenomenon, the minimum probability in the spatio-temporal transition probability matrix for any land cover type remaining the same is chosen as the threshold to identify the unrealistic land cover transitions. For example, in this study, 0.095 was used as the threshold to identify unrealistic changes, which was the smallest transition probability for a land cover type to remain unchanged in Wuhan during 2000–2013 (Refer to Table 2 for details). For the land cover transition of pixel  $u$  between year  $t - 1$  and year  $t$ , the algorithm examines if the probability of such transition in the given spatial context is realistic. If the transition probability is smaller than the predefined threshold, the land cover type of at year  $t$  is modified to the land cover type with the maximum joint transition probability.

Changing the land cover type at year  $t$  influences not only the transition probability between year  $t - 1$  and  $t$ , but also the transition probability between year  $t$  and  $t + 1$ . Therefore, based on the assumption of conditional independence, the sought-after conditional probability can be calculated using the naïve Bayesian equation (Li, 2007; Cao et al., 2011) (Fig. 5):

$$\begin{aligned} P\{C(t) = \omega_k | (C(t-1), C(t+1))\} \\ = \frac{P\{C(t) = \omega_k | C(t-1)\}P\{C(t+1) | C(t) = \omega_k\}}{\sum_{k=1}^{k=4} P\{C(t) = \omega_k | C(t-1)\}P\{C(t+1) | C(t) = \omega_k\}} \end{aligned} \quad (3)$$

where  $C(t - 1)$ ,  $C(t)$ , and  $C(t + 1)$  represent the land cover type at year



$P\{C(t + 1) | C(t) = \omega_k\}$  are extracted from the spatio-temporal transition probability matrix. (For interpretation of the references to colour in this figure legend, the reader is referred to the web version of this article.)

$t - 1$ ,  $t$ , and  $t + 1$  respectively, and  $\omega_k (k = 1, 2, 3, 4)$  is the land cover type. The pair-wise conditional probabilities  $P\{C(t) = \omega_k | C(t - 1)\}$  and  $P\{C(t + 1) | C(t) = \omega_k\}$  are extracted from the spatio-temporal transition probability matrix.

At each iteration of the modification procedure, the land cover sequence of each pixel is examined and modified by the above algorithm. At the end of each iteration, the land cover trajectories are summarized. The iterative modification ends till the cumulative percentage of the top 20 land cover trajectories reaching 99.90%. Details about land cover trajectories are in Section 2.6.

## 2.5. Assessment of annual change detection

For each annual change detection, we randomly selected 100 pixels that were modified by the STLCF and 100 pixels that were not modified. The samples used for the annual change detection were not the same as samples for the classification, because samples used to validate classification may not be modified by STLCF. The overall accuracy of the land cover change detection was calculated with one-year tolerance, based on the visual interpretation of land cover changes in 200 selected pixels assisted by available high-resolution Google Earth images. To evaluate the performance of STLCF, we conducted the accuracy assessment of annual change detection on both the initial land cover maps and land cover maps modified by STLCF.

## 2.6. Analyses of annual land cover dynamics

To analyze annual land cover dynamics in the study area, the annual land cover change rate was calculated as the ratio of the number of pixels experienced a certain type of land cover change to the total number of pixels in the study area. The temporal trend of the annual land cover change rate was then analyzed. In addition, we derived the land cover trajectories for each pixel. Land cover trajectories characterize the temporal land cover change events in the entire time series, instead of searching for the single-change events between maps of two dates (Kennedy et al., 2007; Wang et al., 2012; Carmona and Nahuelhual, 2012).

A land cover trajectory can be coded in different forms (e.g. in values or letters) for each pixel in the time series of land cover maps (Wang et al., 2012; Zomlot et al., 2017). We used the land cover type number ranging from 1 to 4 as trajectory codes. The trajectory did not include the land cover types in the first year and the last year, because the beginning and the end of time series were not modified. To simplify the expression of land cover trajectories, we compressed the 12-year land cover trajectory by showing the distinct land cover types in the time series. For example, if the 12-year trajectory was 444444444111, the trajectory was compressed as 41. Thus, the lengths of the land cover trajectories varied with pixels, depending on how many land cover changes occurred during the study period.

In this study, the land cover trajectories were summarized throughout the study area for the initial and the modified land cover

**Fig. 5.** Illustration of the naïve Bayesian equation. The  $3 \times 3$  spatial neighborhood of a given pixel (including the pixel itself) is in blue. A given pixel in the previous year ( $t - 1$ ) is in yellow, the pixel in the current year ( $t$ ) is in green, and the pixel in the next year ( $t + 1$ ) is in red.  $C(t-1)$ ,  $C(t)$ , and  $C(t + 1)$  represent the land cover type at year  $t - 1$ ,  $t$ , and  $t + 1$  respectively, and  $\omega_k (k = 1, 2, 3, 4)$  is the land cover type. The conditional probabilities  $P\{C(t) = \omega_k | C(t - 1)\}$  and

maps respectively. Since studies have shown that trajectory analysis provides a new approach to validate the rationality of multi-date land cover changes (Liu and Zhou, 2004), we compared the number of land cover trajectories before and after the application of the STLCF to evaluate the performance of STLCF in removing unrealistically frequent land cover changes.

## 3. Results

### 3.1. Initial classification

**Fig. 6** demonstrates the annual land cover maps of 2000–2013 from the initial classification. The overall accuracy varied with years, ranging from 87.50% in 2012 to 92.85% in 2008. The mean overall accuracy for classification was 91.22%. The lower classification accuracy in 2012 was primarily resulted from the higher cloud cover in the base image; croplands under the thin clouds were classified as bare land. The urban expansion was obviously shown in the time series of land cover maps. The satisfying initial classification results ensured the validity of the spatio-temporal transition probability matrix.

With four land cover types and twelve years (without the first and the last year), the initial annual land cover maps generated 5297 land cover trajectories in total. The vast majority of these trajectories were illogical, showing frequent land cover changes during the study period. The static trajectories with the stable land cover types accounted for 66.15% of all pixels in the study area (Table 1). The top 20 land cover trajectories accounted for 90.14% of pixels in the study area.

**Table 2** summarizes the spatio-temporal transition probability matrix derived from the initial classification, with the unrealistic land cover transitions highlighted with underscores. The land cover changes were greatly affected by the land cover types in the neighborhood. As expected, in the area dominated by built-up areas, the major changes were conversions from the other land cover types to built-up areas. The conversion from built-up areas to vegetation was more likely to happen in the area dominated by vegetation than in the area dominated by built-up areas. Similarly, the conversion from water to built-up areas was more likely to happen in the built-up neighborhood.

### 3.2. Performance of the STLCF

Four iterations of the modification were applied until the predefined goal was achieved, which was the top 20 major land cover trajectories accounting for at least 99.90% of the pixels. After the modification, the number of land cover trajectories was reduced from 5297 to 291. **Table 3** demonstrates the percentage and the cumulative percentage of the top 20 land cover trajectories. The most significant non-static land cover change trajectory in the study area was the conversion from vegetation to built-up areas, accounting for 3.15% of the pixels. 0.40% of pixels experienced the conversion from built-up areas to vegetation (including 0.30% built-up – vegetation, 0.08% built-up - vegetation - built-up, and 0.02% vegetation – built-up – vegetation). Additionally,

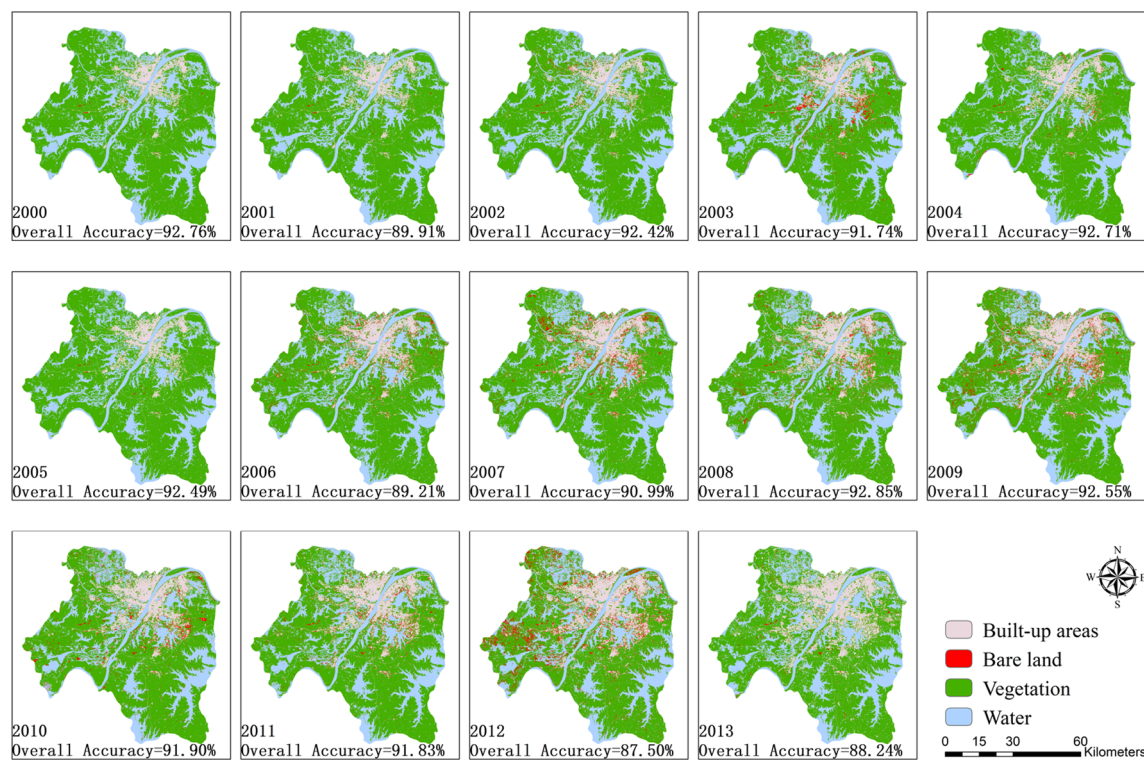


**Fig. 6.** The initial land cover maps of 2000–2013 produced with the DT classifier. The overall accuracy of annual land cover classification is shown in each map.

**Table 1**  
The top 20 land cover trajectories derived from the initial land cover maps.

Trajectory	Percent	Cumulative Percent
1 Vegetation	41.28%	41.28%
2 Water	20.39%	61.67%
3 Built-up areas	4.48%	66.15%
4 Vegetation – Bare land – Vegetation	3.45%	69.60%
5 Vegetation – Bare land	3.17%	72.77%
6 Vegetation – Built-up areas	3.05%	75.82%
7 Vegetation – Water	2.51%	78.33%
8 Water – Vegetation – Water	2.04%	80.37%
9 Vegetation – Water – Vegetation	1.82%	82.19%
10 Water – Vegetation	1.47%	83.66%
11 Vegetation – Bare land – Built-up areas	1.01%	84.67%
12 Vegetation – Bare land – Vegetation - Built-up areas	0.84%	85.51%
13 Vegetation – Bare land – Vegetation – Bare land	0.80%	86.31%
14 Vegetation – Water – Vegetation - Water	0.77%	87.08%
15 Vegetation – Bare land – Vegetation – Bare land – Vegetation	0.64%	87.72%
16 Water – Vegetation - Water- Vegetation – Water	0.61%	88.33%
17 Vegetation – Built-up areas – Vegetation	0.58%	88.91%
18 Water – Vegetation – Water – Vegetation	0.46%	89.37%
19 Vegetation – Built-up areas - Vegetation – Built-up areas	0.39%	89.76%
20 Built-up areas – Vegetation – Built-up areas	0.38%	90.14%

0.04% of the pixels experienced the conversion from built-up areas to water. In total, 7.86% of the pixels in the study area experienced one land cover change, 0.5% of the pixels experienced twice land cover changes, and about 0.07% of the pixels experienced more than twice land cover changes.

Considerable improvements in rationalizing land cover trajectories were achieved through the STLCF. Fig. 7 illustrates three examples of pixels that experienced frequent and illogical land cover changes during the study period, which were mainly caused by the mis-registration of

**Table 2**

Spatio-temporal transition probability matrix derived from the initial land cover maps of 2000 – 2013. The unrealistic land cover transitions (probabilities < 0.095) are highlighted with underscores.

Dominant type in the t neighborhood		t + 1			
		Built-up areas	Bare land	Vegetation	Water
Built-up areas	Built-up areas	0.948	<u>0.018</u>	<u>0.030</u>	<u>0.004</u>
	Bare land	0.408	0.278	0.299	<u>0.015</u>
	Vegetation	0.279	0.153	0.554	<u>0.014</u>
	Water	0.164	<u>0.093</u>	0.192	0.551
Bare land	Built-up areas	0.822	<u>0.072</u>	0.099	<u>0.007</u>
	Bare land	0.177	0.209	0.588	<u>0.026</u>
	Vegetation	0.098	0.157	0.719	<u>0.026</u>
	Water	<u>0.049</u>	<u>0.080</u>	0.228	0.643
Vegetation	Built-up areas	0.653	<u>0.058</u>	0.278	<u>0.011</u>
	Bare land	<u>0.077</u>	0.144	0.763	<u>0.016</u>
	Vegetation	<u>0.014</u>	<u>0.023</u>	0.947	<u>0.016</u>
	Water	<u>0.010</u>	<u>0.011</u>	0.285	0.694
Water	Built-up areas	0.614	<u>0.030</u>	0.135	0.221
	Bare land	<u>0.064</u>	0.095	0.431	0.410
	Vegetation	<u>0.015</u>	<u>0.026</u>	0.676	0.283
	Water	<u>0.004</u>	<u>0.003</u>	<u>0.033</u>	0.960

multi-date images and misclassification of mixed spectra. After the application of the STLCF, the mis-classification and mis-registration were corrected, and the land cover trajectories became consistent and logical.

We then compared the overall accuracy of annual change detection with one-year tolerance for the modified land cover maps against those for the initial land cover maps (Fig. 8). The overall accuracy of annual change detection for the modified land cover maps ranged from 88.0% to 94.5%, with the mean overall accuracy of 91.6%. For the initial land cover maps, the accuracy ranged from 83.5% to 88.0%, with the mean overall accuracy of 85.7%. The comparison indicated the reliability of

**Table 3**

The top 20 land cover trajectories, the percentage, and the cumulative percentage, derived from annual land cover maps of 2001–2012 after the application of the STLCF.

Trajectory	Percent	Cumulative Percent
1 Vegetation	58.52%	58.52%
2 Water	26.94%	85.46%
3 Built-up areas	6.09%	91.55%
4 Vegetation – Built-up areas	3.15%	94.70%
5 Vegetation – Water	2.84%	97.54%
6 Water – Vegetation	1.13%	98.67%
7 Water – Built-up areas	0.33%	99.00%
8 Built-up areas – Vegetation	0.30%	99.30%
9 Water – Vegetation – Built-up areas	0.17%	99.47%
10 Water – Vegetation – Water	0.08%	99.55%
11 Built-up areas – Vegetation – Built-up areas	0.08%	99.63%
12 Vegetation – Water – Vegetation	0.06%	99.69%
13 Built-up areas - Water	0.04%	99.73%
14 Bare land – Vegetation	0.03%	99.76%
15 Vegetation – Bare land – Vegetation	0.03%	99.79%
16 Vegetation – Bare land – Built-up areas	0.03%	99.82%
17 Bare land	0.02%	99.84%
18 Vegetation – Bare land	0.02%	99.86%
19 Vegetation – Built-up areas – Vegetation	0.02%	99.88%
20 Bare land – Built-up areas	0.02%	99.90%

the initial classification and the effective modifications by the STLCF.

### 3.3. Annual urban land cover dynamics

Fig. 9 demonstrates the spatial distribution of land cover trajectories derived from the modified annual land cover maps from 2001 to 2012. The pronounced transition from vegetation to built-up areas can be found on the fringe of the metropolitan area. In the northwest of the study area, vast vegetated areas were converted to water bodies. Red areas which represent the conversion from water bodies to built-up areas are also obvious in Fig. 9.

Fig. 10 demonstrates the proportion of annual dynamics in urbanization, the conversion to water bodies, vegetation gain, and vegetation loss in the study area, including the rate of the unchanged. Urbanization accelerated since 2004, with the pronounced increasing trend in the conversions from vegetated areas and water bodies to built-up areas. The trend of the vegetation loss and the conversion to water bodies were roughly in agreement with that of the urbanization. The conversion from vegetation to water bodies, mainly ponds, also increased since 2004. As expected, vegetation loss was primarily attributed by the conversion from vegetation to built-up areas. Vegetation decreased drastically through thirteen years, with a minimal gain from water bodies, probably because of the growth of aquatic plants in the ponds or the deterioration of water quality.

## 4. Discussion

### 4.1. Performance of the STLCF

The advantage of the STLCF is to check the temporal consistency and make modifications according to the probabilities calculated from the land cover data in the study area. Thus, the temporal-consistent land cover transitions may vary with cities, and sometimes may be against the general experts' opinions. For example, most studies treated the built-up areas as irreversible, because the conversion from built-up areas to the other land cover types is rare and small in comparison with urbanization-induced land cover changes (Nor et al., 2017). With the increasing attention on the function of vegetation in urban areas, it becomes possible that built-up areas are restored either for recreational purposes or for climate adaptation (Derkzen et al., 2017). In Europe and the US, urban shrinkage offers ample opportunities for re-greening

through urban agriculture and wilding vacant lots (Colding et al., 2013; Kremer et al., 2013; Haase et al., 2014). In this study, the probability of the conversion from built-up areas to vegetation was small when the neighborhood was dominated by built-up areas, but the probability of the conversion from built-up areas to vegetation was beyond the predefined threshold when the neighborhood was dominated by the other land cover types. Therefore, the conversion from built-up areas to vegetation can be found near rivers and lakes, in the reserves and rural areas, mainly caused by the restoration of built-up areas to the park or green belt/wedges along rivers and new roads in the metropolitan areas, and to the cropland and woods in the rural areas. This result agreed with the findings in Huang et al. (2017), which found that the city blocks with high vegetation fractions in Wuhan were distributed in the scenic areas (e.g. East Lake), and rarely in the city center and residential areas.

The spatio-temporal transition probability matrix used in the STLCF also showed that some subtle land cover changes, such as the conversions from water to built-up areas and those from vegetation to water, which may not normally exist in the other cities, occurred in the study area. Lakes shrank because of the preferences of building apartments nearby lakes. In the northeastern Wuhan, large areas of cropland were converted to ponds for fisheries and aquatic plants, driven by economic benefits.

The effect of STLCF was evaluated by both the accuracy of annual change detection and the number of land cover change trajectories. The mean overall accuracy of annual change detection for the land cover maps modified by the STLCF was 91.6%, about 6% higher than those before the implementation of STLCF. The mean overall accuracy in our study was comparable to the previous studies of annual land cover dynamics (Table 4), which also conducted a temporal consistency check but focused on the conversions to built-up areas /impervious surface. Moreover, the amount of land cover trajectories was substantially reduced through the STLCF method. The 20 major land cover trajectories accounted for over 99.90% of the pixels in the study area, indicating that land cover maps became more consistent within its spatio-temporal context.

Errors of the STLCF were primarily resulted from misclassifications in the initial land cover maps (discussed in Section 4.3). On the other hand, the transitions with the probabilities smaller than the threshold may actually happen in the study area. After the implementation of STLCF, these rare transitions were modified into the 'wrong' land cover types to make the land cover trajectories consistent. Such errors were inevitable for temporal filters. But since these transitions were rare in the study area, the impacts of such errors on the overall accuracy of the modified land cover maps should be minimal.

### 4.2. Parameters in the STLCF

The implementation of the STLCF required a predefined spatial neighborhood and a threshold to identify unrealistic land cover changes. To select the appropriate spatial neighborhood, we computed spatio-temporal transition matrixes with the spatial window size of  $3 \times 3$ ,  $5 \times 5$ , and  $7 \times 7$  pixels, respectively. Table 1 in Appendix shows spatio-temporal transition matrixes with the spatial window size of  $5 \times 5$  and  $7 \times 7$  pixels. With the increasing spatial window sizes, the probabilities of stable land cover transitions also increased. The differences in transition probabilities among these three matrixes were not pronounced. Using the same rule to define threshold as we did for the spatial window size of  $3 \times 3$ , we found that the unrealistic land cover transitions identified for the increased spatial window sizes were identical, except for the spatial window size of  $7 \times 7$  the transition from built-up areas to vegetation in the water neighborhood was unrealistic whereas this transition was realistic in the other two matrixes. Given the results of the comparison in spatio-temporal transition matrixes, we hypothesized that land cover maps modified with the spatial window size of  $5 \times 5$  would be similar to those modified with the spatial

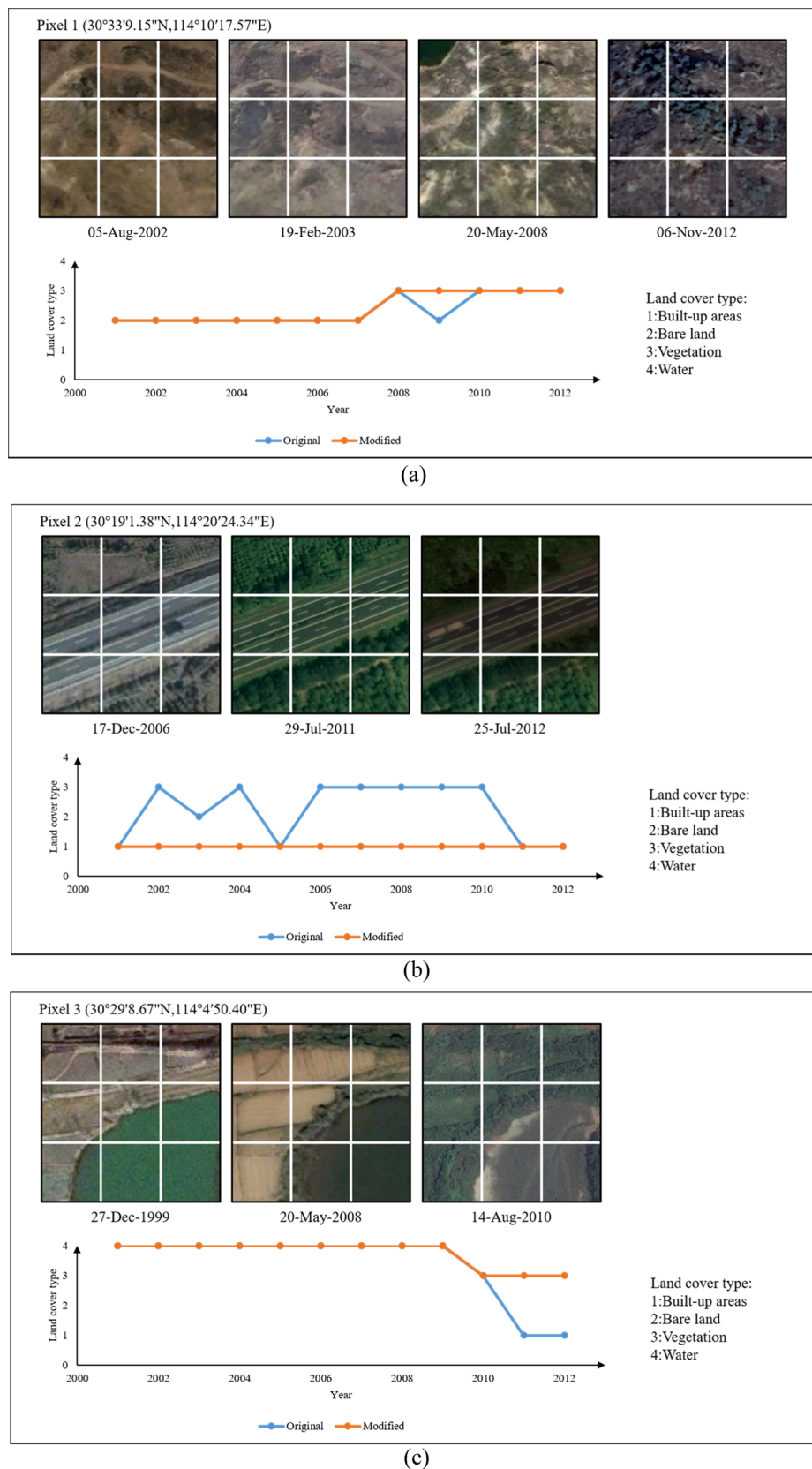


**Fig. 7.** Multi-date Google Earth images of three sample pixels within the  $3 \times 3$  spatial neighborhood, and Land cover trajectories of the sample pixels. Land cover trajectories derived from the initial land cover maps were compared against those derived from the land cover maps modified by STLCF. Pixel (a) is located in bare land, pixel (b) is located in a highway, and pixel (c) is located in a cropland.

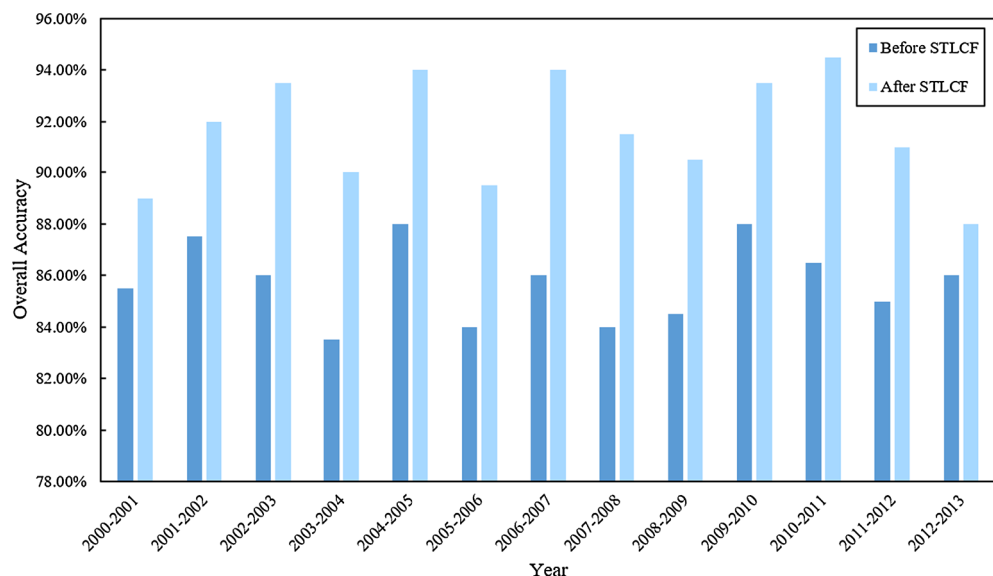


**Fig. 8.** Comparison of the overall accuracy of the annual change detection with one-year tolerance for the land cover maps modified by the STLCF against those for the initial land cover maps.

window size of  $3 \times 3$ , but STLCF with the spatial window size of  $5 \times 5$  would cost more computation time; land cover maps modified with the spatial window size of  $7 \times 7$  would be smoother by removing certain subtle changes. Therefore, in this study we defined the spatial neighborhood as  $3 \times 3$  pixels.

We used the minimum probability in the spatio-temporal transition probability matrix for any land cover type remaining the same as the threshold, because land cover change in time is a relatively rare phenomenon. The improvement in the annual change detection accuracy after the implementation of STLCF suggested that the selected threshold was effective to identify the unrealistic transitions while kept a few

actual transitions that did not happen very often. The other way was to iteratively search for the optimal threshold that could yield the highest accuracy of annual change detection. As the STLCF computed on both spatial and temporal dimensions, iteratively searching for the optimal threshold is computationally intensive. Parallel computing techniques can be used to improve the efficiency of such task and the computing time can be largely reduced. The choice of the threshold is of great importance to the performance of STLCF. The higher value of the threshold would smooth the land cover trajectories, losing uncommon but actually-happened land cover changes; the lower value of the threshold would keep more frequent land cover changes. Optimizing

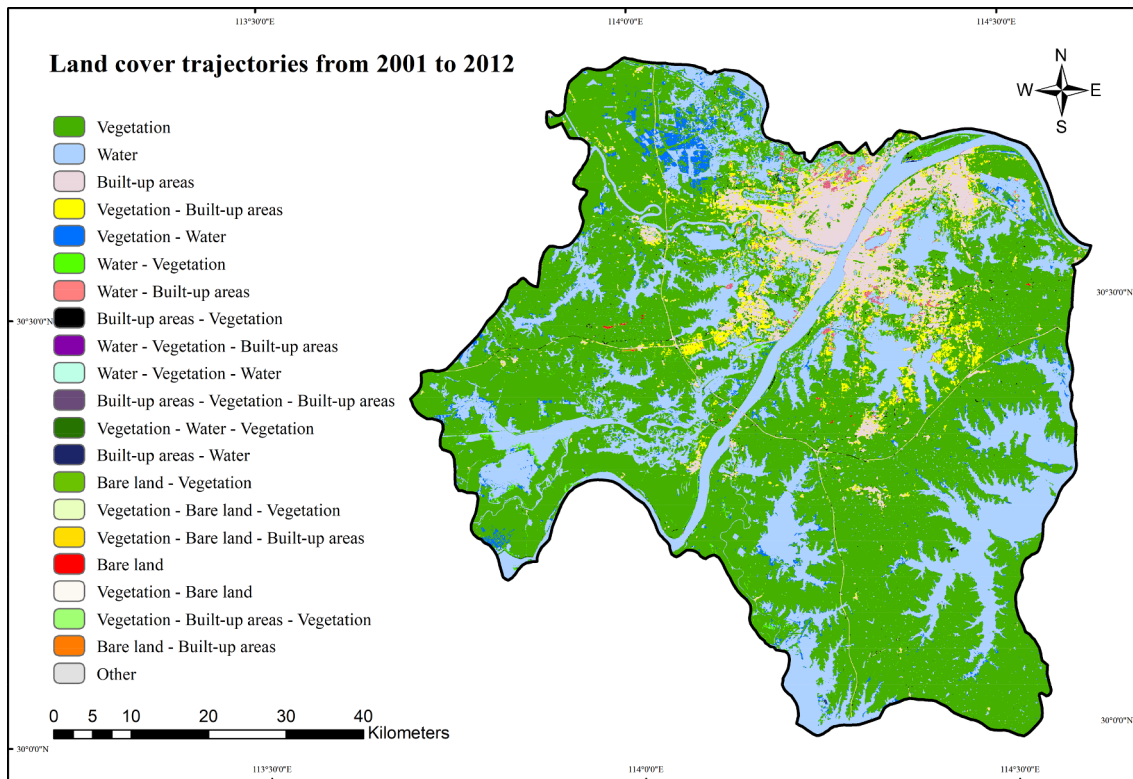


**Fig. 9.** The spatial distribution of land cover trajectories from 2001 to 2012 derived from the modified land cover maps.

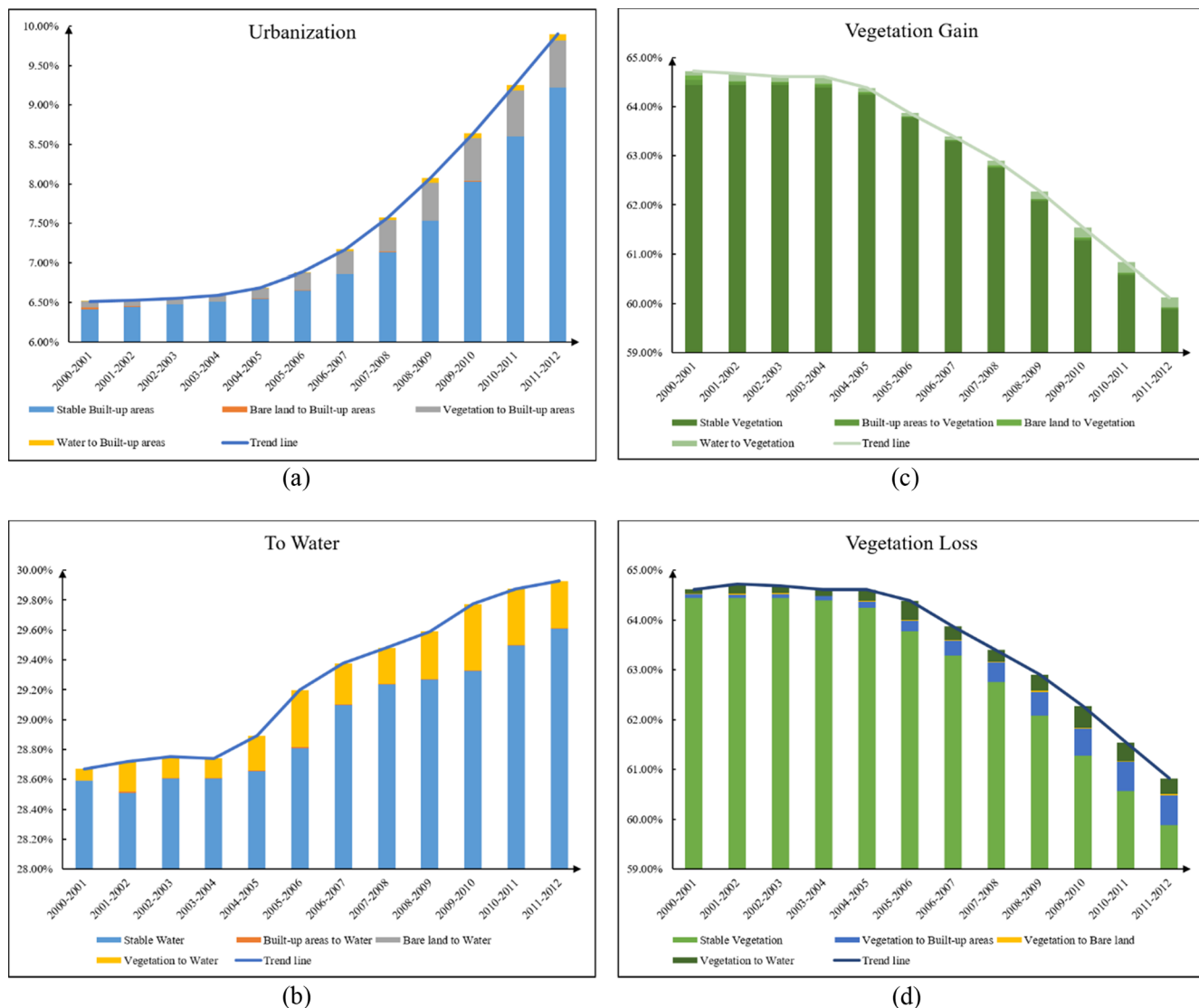


**Fig. 10.** The proportion of annual change in (a) urbanization, (b) the conversion to water bodies, (c) vegetation gain, and (d) vegetation loss in the study area.

**Table 4**

Comparison of the (mean) overall accuracy of annual change detection for the land cover maps modified by the STLCF against that of the previous studies.

Study	Study period (year)	With one-year tolerance (yes/no)	(Mean) overall accuracy
Our study	2001–2012	yes	91.6%
Li et al. (2017)	1984–2014	no	83%
Song et al. (2016)	1986–2008	yes	99.7%
Li et al. (2018)	1985–2015	yes	90%

the threshold selection will be one of our future tasks to improve the performance of STLCF.

#### 4.3. Impacts of the initial classification

The DT method was employed for the classification instead of a more advanced classification method (e.g. random forest), because it is non-parametric and intuitive (Schneider, 2012), and also because we used four land cover types that have distinct spectral-temporal characteristics (Pflugmacher et al., 2019). Although the initial classification

achieved the average accuracy of 91.22%, the inaccurate classification still existed, and was the primary source of thousands of land cover trajectories derived from the initial classification. The accuracy of the initial classification varied with years, since the time of the image acquisition, the number of images used within a year, and the proportion of cloud cover would affect land cover mapping. Additionally, when the mapped land cover is finer than the spatial resolution, the pixels are easily misclassified due to the mixed spectra (Settle and Drake, 1993; Wetherley et al., 2017). For example, the bridges on rivers or lakes were classified as built-up areas in some years, but classified as water in the other years, resulting in the transitions from built-up areas to water bodies. Moreover, it was challenging to discriminate between bare land with wild grasses, when buildings were dismantled and the land was vacant for a year or longer. The confusion played an important role in the land cover change from built-up areas to vegetation. The modification may correct some of the misclassifications by considering the spatial and temporal context, but in some other cases the misclassification may be kept to improve the temporal consistency of the land cover trajectories. This study did not evaluate the transport of the uncertainty in the initial classification to the results of STLCF and annual change detection. Future efforts are needed to evaluate the uncertainty in the long-term annual land cover change detection.

#### 4.4. Annual urban land cover dynamics

The primary purpose of analyzing the annual urban land cover dynamics is to capture the rapid development in cities that are driven by the urban planning, land-use policies, and geographical and social-economic conditions (Li et al., 2015; Long et al., 2012; Li et al., 2018). The annual analysis in the study area illustrated that the rate of urbanization was apparently nonlinear. Urbanization accelerated since 2004, because the Rise of Central China Plan was adopted by the People's Republic of China in 2004 and Hubei province was covered by this policy (Zhang et al., 2018). We also found that in addition to the vegetation loss, urbanization was associated with the increasing trend in the conversion from water to built-up areas. Interestingly, Regulations of Wuhan Municipality on the protection of lakes was established in 2001 and a few amendments were made after that (Liu, 2018), but the response of land cover changes to this regulation was not obvious during the study period.

The STLCF is applicable to any multi-date land cover maps at different scales, facilitating the creation of dense, consistent, long-term land cover datasets. By capturing land cover change on a yearly or even more frequent basis, the nonlinear land cover changes can be analyzed over time, including the acceleration and thresholds hypothesized for complex ecosystems (Sexton et al., 2013). Moreover, land cover change can be more explicitly linked with annual changes in economic, social, environmental, and management factors. A better understanding of evolving land management techniques may be achieved through trajectory analysis of land cover changes.

#### 5. Conclusion

The analyses of annual urban land cover dynamics can capture rapid

#### Appendix

(see Table A1).

**Table A1**

Spatio-temporal transition matrixes with the spatial window size of  $5 \times 5$  (a) and  $7 \times 7$  (b) pixels. The unrealistic land cover transitions (probabilities  $< 0.117$  for the spatial window size of  $5 \times 5$ ; probabilities  $< 0.130$  for the spatial window size of  $7 \times 7$ ) are highlighted with underscores.

(a) $5 \times 5$					
Dominant type in the neighborhood	t	t + 1	Bare land	Vegetation	Water
Built-up areas	Built-up areas	0.959	<u>0.016</u>	<u>0.023</u>	<u>0.002</u>
	Bare land	0.395	0.288	0.306	<u>0.011</u>
	Vegetation	0.240	0.135	0.615	<u>0.010</u>
	Water	0.157	<u>0.084</u>	0.163	0.596
Bare land	Built-up areas	0.843	<u>0.067</u>	<u>0.085</u>	<u>0.005</u>
	Bare land	0.185	0.219	0.575	<u>0.021</u>
	Vegetation	0.094	0.142	0.749	0.015
	Water	<u>0.063</u>	<u>0.082</u>	0.215	0.640
Vegetation	Built-up areas	0.736	<u>0.054</u>	0.201	<u>0.009</u>
	Bare land	<u>0.097</u>	0.156	0.731	<u>0.016</u>
	Vegetation	<u>0.013</u>	<u>0.022</u>	0.950	<u>0.015</u>
	Water	<u>0.010</u>	<u>0.010</u>	0.222	0.758
Water	Built-up areas	0.673	<u>0.037</u>	0.120	0.170
	Bare land	<u>0.087</u>	0.117	0.483	0.313
	Vegetation	<u>0.017</u>	<u>0.029</u>	0.720	0.234
	Water	<u>0.004</u>	<u>0.003</u>	<u>0.028</u>	0.965
(b) $7 \times 7$					
Dominant type in the neighborhood	t	t + 1	Bare land	Vegetation	Water

(continued on next page)

**Table A1 (continued)**

Built-up areas	Built-up areas	0.963	<b>0.015</b>	<b>0.021</b>	<b>0.001</b>
	Bare land	0.373	<b>0.296</b>	0.320	<b>0.011</b>
	Vegetation	0.210	<b>0.128</b>	0.653	<b>0.009</b>
	Water	0.135	<b>0.074</b>	0.159	0.632
Bare land	Built-up areas	0.860	<b>0.062</b>	0.075	0.003
	Bare land	0.192	0.222	0.568	<b>0.018</b>
	Vegetation	<b>0.092</b>	0.132	0.763	<b>0.013</b>
	Water	<b>0.067</b>	<b>0.081</b>	0.208	0.644
Vegetation	Built-up areas	0.778	<b>0.050</b>	0.163	<b>0.009</b>
	Bare land	<b>0.110</b>	0.165	0.710	<b>0.015</b>
	Vegetation	<b>0.013</b>	<b>0.022</b>	0.951	<b>0.014</b>
	Water	<b>0.010</b>	<b>0.009</b>	0.189	0.792
Water	Built-up areas	0.708	<b>0.038</b>	<b>0.114</b>	0.140
	Bare land	<b>0.098</b>	0.130	0.508	0.264
	Vegetation	<b>0.018</b>	<b>0.031</b>	0.752	0.199
	Water	<b>0.004</b>	<b>0.003</b>	<b>0.026</b>	0.967

## References

- Cai, Shanshan, Liu, Desheng, Sulla-Menashe, Damien, Friedl, Mark A., 2014. Enhancing MODIS land cover product with a spatial-temporal modeling algorithm. *Remote Sens. Environ.* 147, 243–255. <https://doi.org/10.1016/j.rse.2014.03.012>.
- Cao, Guofeng, Kyriakidis, Phaedon C., Goodchild, Michael F., 2011. Combining spatial transition probabilities for stochastic simulation of categorical fields. *Int. J. Geograph. Inform. Sci.* 25 (11), 1773–1791. <https://doi.org/10.1080/13658816.2010.528421>.
- Carmona, A., Nahuelhual, L., 2012. Combining land transitions and trajectories in assessing forest cover change. *Appl. Geogr.* 32 (2), 904–915. <https://doi.org/10.1016/j.apgeog.2011.09.006>.
- Chai, Baohui, Li, Peijun, 2018. Annual urban expansion extraction and spatio-temporal analysis using landsat time series data: a case study of Tianjin, China. *IEEE J. Sel. Top. Appl. Earth Obs. Remote Sens.* 11 (8), 2644–2656. <https://doi.org/10.1109/JSTARS.2018.2829525>.
- Churkina, G., 2008. Modeling the carbon cycle of urban systems. *Ecol. Model.* 216, 107–113.
- Clark, Matthew L., Mitchell Aide, T., Ricardo Grau, H., Riner, George, 2010. A scalable approach to mapping annual land cover at 250 m using MODIS time series data: a case study in the dry chaco Ecoregion of South America. *Remote Sens. Environ.* 114 (11), 2816–2832. <https://doi.org/10.1016/j.rse.2010.07.001>.
- Colding, Johan, Barthel, Stephan, Bendt, Pim, Snep, Robbert, van der Knaap, Wim, Ernstson, Henrik, 2013. Urban green commons: insights on urban common property systems. *Global Environ. Change* 23 (5), 1039–1051. <https://doi.org/10.1016/j.gloenvcha.2013.05.006>.
- Derkzen, Marthe L., van Teeffelen, Astrid JA, Nagendra, Harini, Verburg, Peter H., 2017. Shifting roles of urban green space in the context of urban development and global change. *Curr. Opin. Environ. Sustain.* 29 (December), 32–39. <https://doi.org/10.1016/j.cosust.2017.10.001>.
- Dong, Na., You, Lan, Cai, Wenjia, Li, Gang, Lin, Hui, 2018. Land use projections in China under global socioeconomic and emission scenarios: utilizing a scenario-based land-use change assessment framework. *Global Environ. Change* 50 (May), 164–177. <https://doi.org/10.1016/j.gloenvcha.2018.04.001>.
- Friedl, Mark A., Sulla-Menashe, Damien, Tan, Bin, Schneider, Annemarie, Ramankutty, Navin, Sibley, Adam, Huang, Xiaoman, 2010. MODIS collection 5 global land cover: algorithm refinements and characterization of new datasets. *Remote Sens. Environ.* 114 (1), 168–182. <https://doi.org/10.1016/j.rse.2009.08.016>.
- Georgescu, M., Morefield, P.E., Bierwagen, B.G., Weaver, C.P., 2014. Urban adaptation can roll back warming of emerging Megopolitan regions. *Proc. Natl. Acad. Sci.* 111 (8), 2909–2914. <https://doi.org/10.1073/pnas.1322280111>.
- Gong, Peng, Liang, Song, Carlton, Elizabeth J., Jiang, Qingwu, Jianyong, Wu., Wang, Lei, Remais, Justin V., 2012. Urbanisation and health in China. *Lancet* 379 (9818), 843–852. [https://doi.org/10.1016/S0140-6736\(11\)61878-3](https://doi.org/10.1016/S0140-6736(11)61878-3).
- Guan, Qingfeng, Shi, Xuan, Huang, Maoqing, Lai, Chenggang, 2016. A hybrid parallel cellular automata model for urban growth simulation over GPU/CPU heterogeneous architectures. *Int. J. Geograph. Inform. Sci.* 30 (3), 494–514. <https://doi.org/10.1080/13658816.2015.1039538>.
- Haase, Dagmar, Haase, Ansgret, Rink, Dieter, 2014. Conceptualizing the nexus between urban shrinkage and ecosystem services. *Landscape Urban Plan.* 132 (December), 159–169. <https://doi.org/10.1016/j.landurbplan.2014.09.003>.
- He, Yaqian, Lee, Eungul, Warner, Timothy A., 2017. A time series of annual land use and land cover maps of China from 1982 to 2013 generated using AVHRR GIMMS NDVI3g data. *Remote Sens. Environ.* 199, 201–217. <https://doi.org/10.1016/j.rse.2017.07.010>.
- Huang, Xin, Wen, Dawei, Li, Jiayi, Qin, Rongjun, 2017. Multi-level monitoring of subtle urban changes for the megacities of China using high-resolution multi-view satellite imagery. *Remote Sens. Environ.* 196 (July), 56–75. <https://doi.org/10.1016/j.rse.2017.05.001>.
- Jamali, Sadegh, Jönsson, Per, Eklundh, Lars, Ardö, Jonas, Seaquist, Jonathan, 2015. Detecting changes in vegetation trends using time series segmentation. *Remote Sens. Environ.* 156, 182–195. <https://doi.org/10.1016/j.rse.2014.09.010>.
- Kennedy, Robert E., Cohen, Warren B., Schroeder, Todd A., 2007. Trajectory-based change detection for automated characterization of forest disturbance dynamics. *Remote Sens. Environ.* 110 (3), 370–386. <https://doi.org/10.1016/j.rse.2007.03.010>.
- Kremer, Peleg, Hamstead, Zoé A., McPhearson, Timon, 2013. A social-ecological assessment of vacant lots in New York City. *Landscape Urban Plan.* 120, 218–233. <https://doi.org/10.1016/j.landurbplan.2013.05.003>.
- Li, Weidong, 2006. Transiogram: a spatial relationship measure for categorical data. *Int. J. Geograph. Inform. Sci.* 20 (6), 693–699. <https://doi.org/10.1080/13658810600607816>.
- Li, Weidong, 2007. Markov chain random fields for estimation of categorical variables. *Math. Geol.* 39 (3), 321–335. <https://doi.org/10.1007/s11004-007-9081-0>.
- Li, Xuecao, Gong, Peng, Liang, Lu., 2015. A 30-year (1984–2013) record of annual urban dynamics of Beijing city derived from landsat data. *Remote Sens. Environ.* 166, 78–90. <https://doi.org/10.1016/j.rse.2015.06.007>.
- Li, Guangdong, Sun, Siao, Fang, Chuanglin, 2018a. The varying driving forces of urban expansion in China: insights from a spatial-temporal analysis. *Landscape Urban Plan.* 174, 63–77. <https://doi.org/10.1016/j.landurbplan.2018.03.004>.
- Li, Xuecao, Zhou, Yuyu, Zhengyuan Zhu, Lu., Liang, Bailang Yu, Cao, Wenting, 2018b. Mapping annual urban dynamics (1985–2015) using time series of landsat data. *Remote Sens. Environ.* 216, 674–683. <https://doi.org/10.1016/j.rse.2018.07.030>.
- Li, Desheng, Cai, Shanshan, 2012. A spatial-temporal modeling approach to reconstructing land-cover change trajectories from multi-temporal satellite imagery. *Ann. Assoc. Am. Geogr.* 102 (6), 1329–1347. <https://doi.org/10.1080/00045608.2011.596357>.
- Li, Xiaoping, Guohua, Hu., Chen, Yimin, Li, Xia, Xiaocong, Xu., Li, Shaoying, Pei, Fengsong, Wang, Shaolian, 2018. High-resolution multi-temporal mapping of global urban land using landsat images based on the Google earth engine platform. *Remote Sens. Environ.* 209, 227–239. <https://doi.org/10.1016/j.rse.2018.02.055>.
- Li, H., Zhou, Q., 2004. Accuracy analysis of remote sensing change detection by rule-based rationality evaluation with post-classification comparison. *Int. J. Remote Sens.* 25 (5), 1037–1050. <https://doi.org/10.1080/0143116031000150004>.
- Liu Qi. "Dilemmas and Way Out of the Environmental Legislation of Wuhan Municipal Government" 31 (5): pp. 182–184; 2018.
- Long, Ying, Yizhen, Gu., Han, Haoying, 2012. Spatiotemporal heterogeneity of urban planning implementation effectiveness: evidence from five urban master plans of Beijing. *Landscape Urban Plan.* 108 (2–4), 103–111. <https://doi.org/10.1016/j.landurbplan.2012.08.005>.
- Nor, A.N., Corstanje, R., Harris, J.A., Brewer, T., 2017. Impact of rapid urban expansion on green space structure. *Ecol. Indicat.* 81, 274–284. <https://doi.org/10.1016/j.ecolind.2017.05.031>.
- Pflugmacher, Dirk, Rabe, Andreas, Peters, Mathias, Hostert, Patrick, 2019. Mapping pan-European land cover using landsat spectral-temporal metrics and the European LUCAS survey. *Remote Sens. Environ.* 221, 583–595. <https://doi.org/10.1016/j.rse.2018.12.001>.
- Scaramuzza, P., E. Micićević, and G. Chander. n.d. "SLC Gap-Filled Products Phase One Methodology." Landsat Technical Notes, Sioux Falls, SD, USA, Mar. 2004.
- Schneider, Annemarie, 2012. Monitoring land cover change in urban and peri-urban areas using dense time stacks of landsat satellite data and a data mining approach. *Remote Sens. Environ.* 124, 689–704. <https://doi.org/10.1016/j.rse.2012.06.006>.
- Schneider, Annemarie, Friedl, Mark A., Potere, David, 2010. Mapping global urban areas using MODIS 500-m data: new methods and datasets based on 'urban ecoregions'. *Remote Sens. Environ.* 114 (8), 1733–1746. <https://doi.org/10.1016/j.rse.2010.03.003>.
- Seto, Karen C., Fragkias, Michail, 2005. Quantifying spatiotemporal patterns of urban land-use change in four cities of China with time series landscape metrics. *Landscape Ecol.* 20 (7), 871–888. <https://doi.org/10.1007/s10980-005-5238-8>.

- Settle, J.J., Drake, N.A., 1993. Linear mixing and the estimation of ground cover proportions. *Int. J. Remote Sens.* 14 (6), 1159–1177. <https://doi.org/10.1080/01431169308904402>.
- Sexton, Joseph O., Urban, Dean L., Donohue, Michael J., Song, Conghe, 2013b. Long-term land cover dynamics by multi-temporal classification across the landsat-5 record. *Remote Sens. Environ.* 128, 246–258. <https://doi.org/10.1016/j.rse.2012.10.010>.
- Sexton, Joseph O., Song, Xiao-Peng, Huang, Chengquan, Channan, Saurabh, Baker, Matthew E., Townshend, John R., 2013a. Urban growth of the Washington, D.C.–Baltimore, MD metropolitan region from 1984 to 2010 by annual, landsat-based estimates of impervious cover. *Remote Sens. Environ.* 129, 42–53. <https://doi.org/10.1016/j.rse.2012.10.025>.
- Song, Xiao-Peng, Sexton, Joseph O., Huang, Chengquan, Channan, Saurabh, Townshend, John R., 2016. Characterizing the magnitude, timing and duration of urban growth from time series of landsat-based estimates of impervious cover. *Remote Sens. Environ.* 175, 1–13. <https://doi.org/10.1016/j.rse.2015.12.027>.
- Tan, Ronghui, Liu, Yaolin, Liu, Yanfang, He, Qingsong, Ming, Licai, Tang, Shuohua, 2014. Urban growth and its determinants across the Wuhan urban agglomeration, central China. *Habit. Int.* 44, 268–281. <https://doi.org/10.1016/j.habitatint.2014.07.005>.
- Wang, Dongchuan, Gong, Jianhua, Chen, Lidong, Zhang, Lihui, Song, Yiquan, Yue, Yujuan, 2012. Spatio-temporal pattern analysis of land use/cover change trajectories in Xixe watershed. *Int. J. Appl. Earth Observ. Geoinform.* 14 (1), 12–21. <https://doi.org/10.1016/j.jag.2011.08.007>.
- Wang, Jie, Zhao, Yuanyuan, Li, Congcong, Le, Yu., Liu, Desheng, Gong, Peng, 2015. Mapping global land cover in 2001 and 2010 with spatial-temporal consistency at 250m resolution. *ISPRS J. Photogramm. Remote Sens.* 103, 38–47. <https://doi.org/10.1016/j.isprsjprs.2014.03.007>.
- Wehmann, Adam, Liu, Desheng, 2015. A Spatial-temporal contextual markovian kernel method for multi-temporal land cover mapping. *ISPRS J. Photogramm. Remote Sens.* 107, 77–89. <https://doi.org/10.1016/j.isprsjprs.2015.04.009>.
- Wetherley, Erin B., Roberts, Dar A., McFadden, Joseph P., 2017. Mapping spectrally similar urban materials at sub-pixel scales. *Remote Sens. Environ.* 195, 170–183. <https://doi.org/10.1016/j.rse.2017.04.013>.
- Woodcock, Curtis E., and Mutlu Ozdogan. 2012. “Trends in Land Cover Mapping and Monitoring.” In *Land Change Science*, edited by Garik Gutman, Anthony C. Janetos, Christopher O. Justice, Emilio F. Moran, John F. Mustard, Ronald R. Rindfuss, David Skole, Billy Lee Turner, and Mark A. Cochrane, 6:367–77. Dordrecht: Springer Netherlands. [https://doi.org/10.1007/978-1-4020-2562-4\\_21](https://doi.org/10.1007/978-1-4020-2562-4_21).
- Zhang, Yue-Jun, Liu, Zhao, Zhou, Si-Ming, Qin, Chang-Xiong, Zhang, Huan, 2018. The impact of China’s central rise policy on carbon emissions at the stage of operation in road sector. *Econ. Model.* 71, 159–173. <https://doi.org/10.1016/j.economod.2017.12.009>.
- Zomlot, Z., Verbeiren, B., Huysmans, M., Batelaan, O., 2017. Trajectory analysis of land use and land cover maps to improve spatial-temporal patterns, and impact assessment on groundwater recharge. *J. Hydrol.* 554, 558–569. <https://doi.org/10.1016/j.jhydrol.2017.09.032>.